ELSEVIER

Journal of Power Sources 110 (2002) 267–284

JOURNAL OF POWER SOURCES

www.elsevier.com/locate/jpowsour

Mathematical modeling of lithium-ion and nickel battery systems

Parthasarathy M. Gomadam[a], John W. Weidner[a,*], Roger A. Dougal[b], Ralph E. White[a]

[a]*Center for Electrochemical Engineering, Department of Chemical Engineering, University of South Carolina, Columbia, SC 29208, USA*
[b]*Department of Electrical Engineering, University of South Carolina, Columbia, SC 29208, USA*

Abstract

A review of mathematical models of lithium and nickel battery systems developed at the University of South Carolina is presented. Models of Li/Li-ion batteries are reviewed that simulated the behavior of single electrode particles, single electrodes, full cells and batteries (sets of full cells) under a variety of operating conditions (e.g. constant current discharge, pulse discharge, impedance and cyclic voltammetry). Models of nickel battery systems are reviewed that simulate the performance of full cells, as well as the behavior of the nickel hydroxide active material. The ability of these models to predict reality is demonstrated by frequent comparisons with experimental data.

Keywords: Simulations; Impedance; Porous electrode theory; Continuum models

1. Li-ion battery modeling

1.1. Background

Among the rechargeable battery systems available at present, the Li/Li-ion systems provide the highest energy densities [1]. This makes the Li/Li-ion systems the most attractive candidates for electric vehicle and space applications. However, owing to various practical problems associated with Li/Li-ion cells, their commercial use is restricted primarily to small coin cells and 18650 cylindrical cells. In an effort to make the large scale use of these systems workable and safe, mathematical modeling has proved to be an efficient, cost effective tool. The modeling efforts of researchers in the field of Li/Li-ion battery systems are principally based on the isothermal electrochemical model developed by Doyle et al. [1] for galvanostatic discharge of Li/Li-ion cells. In this work, the authors have developed a very general one-dimensional (1D) model applicable to almost any of the existing Li/Li-ion systems. Their model uses porous electrode theory, a macro-homogeneous approach developed by Newman [2], to describe the potential variations in the solid and solution phases. The material balance in the solution phase is described using the concentrated solution theory and in the solid phase using a Fickian diffusion equation in spherical coordinates. Confining only to isothermal conditions, the authors validate their model by demonstrating good agreement with the experimental data [3]. Later, Pals and Newman [4], Song and Evans [5] and Wang et al. [6] extended this model to include an energy balance in order to predict cell temperature. Pals and Newman [4] used an average heat generation method while Song and Evans [5] and Wang et al. [6] used local heat generation terms. An electrochemical-thermal model using local heat generation terms has been shown to be more accurate [7], and includes all the features of the isothermal model developed by Doyle et al. [1] and the additional energy balance included by Song and Evans [5] and Wang et al. [6]. Therefore, it is deemed important at this point to explain the development of such a model for a typical Li-ion system, as explained in the work of Gomadam et al. [7]. This model, either wholly or partly, has been used by researchers for modeling single electrode particles, single electrodes, full cells and batteries (sets of full cells) to simulate various operating conditions like cyclic voltammetry, constant current discharge, pulse discharge and impedance. The problems encountered with Li-ion systems like poor rate capability, thermal runaway, occurrence of undesired side reactions and capacity fade have been addressed using the model.

1.2. System description

A schematic representation of a typical Li-ion cell is shown in Fig. 1. The cell sandwich consists of five regions: the negative electrode current collector made of copper, the porous composite negative insertion electrode, the porous

* Corresponding author. Tel.: +1-803-777-3207; fax: +1-803-777-8265.
E-mail address: weidner@engr.sc.edu (J.W. Weidner).

0378-7753/02/$ – see front matter
PII: S0378-7753(02)00190-8

Nomenclature

a	specific area of an electrode (m^{-1})
A	first parameter in Eq. (46)
A_i	coefficients in Eq. (41)
B	second parameter in Eq. (46)
b	dimensionless parameter as defined in Eq. (40)
c	concentration in a phase (mol/m^3)
C_p	volume averaged specific heat capacity (J/(kg K))
D	diffusion coefficient in a phase (m^2/s)
E_0	formal potential corresponding to Eq. (46) (V)
E_a	Arrhenius activation energy (J/mol)
F	Faraday's constant (96 487 C/mol)
f	mean molar activity coefficient of the electrolyte
h	external heat transfer coefficient ($W/(m^2\ K)$)
i	local current density in a phase (A/m^2)
i_0	exchange current density at an interface (A/m^2)
k	rate constant ($A/(m^2\ (mol/m^3)^{3/2})$)
J	local volumetric transfer current density due to charge transfer (A/m^3)
L	length of the cell (m)
m	outward normal to a boundary (m)
M	molecular mass (kg/mol)
P	generic property defined in Eq. (4)
q	local volumetric heat generation (W/m^3)
$\mathscr{R}$	rate of reaction ($mol/(m^3\ s)$)
R	universal gas constant (8.314 J/(mol K))
r	radial coordinate (m)
S	host site
t	time (s)
t^+	transference number of Li^+ ions in solution
v	specific volume for packing of spheres
V_{eq}	equilibrium cell voltage (V)
x	coordinate along the cell length (m)
y	coordinate along the cell height (m)
z	coordinate along the cell width (m)

Greek symbols

α	transfer coefficient
δ	radius of an electrode particle (m)
ΔH	enthalpy of reaction (J/mol)
ε	volume fraction of a phase
η	surface overpotential (V)
θ	local state of charge
κ	conductivity of the electrolyte (S/m)
κ_D	diffusional conductivity of the electrolyte (A/m)
λ	thermal conductivity (W/(m K))
ρ	density (kg/m^3)
σ	conductivity of the matrix phase (S/m)
ϕ	local potential with respect to Li/Li^+ (V)
χ	volume fraction

Subscripts

−	to the left of an interface
+	to the right of an interface
1	matrix phase
2	solution phase (except in Eqs. (32) and (33) where it corresponds to the lithium deposition side reaction)
a	anodic
amb	ambient
app	applied
c	cathodic
Cu,n	copper current collector–negative electrode interface
D_1	corresponding to solid phase diffusivity
D_2	corresponding to solution phase diffusivity
film	of film
H^+	of H^+
i_0	corresponding to equilibrium exchange current density
j	defined when used
L	when larger particles are controlling
Li	of lithium
Li_2CO_3	of lithium carbonate
NiOOH	of NiOOH
$Ni(OH)_2$	of $Ni(OH)_2$
n	negative electrode
n,s	negative electrode–separator interface
p	positive electrode
p,Al	positive electrode–aluminum current collector interface
ref	reference state
S	when smaller particles are controlling
s	separator
s,p	separator–positive electrode interface
σ	corresponding to solid phase conductivity
κ	corresponding to solution phase conductivity

Superscripts

0	initial
eff	effective
max	maximum
s	surface
brug	Bruggeman exponent

separator, the porous composite positive insertion electrode and the positive electrode current collector made of aluminum. The composite electrodes are made of their active material particles (e.g. MCMB 2528 in the case of negative and $LiCoO_2$ in the case of positive), held together with a PVDF binder and a suitable filler material such as carbon black. From its fully charged state, when the open circuit potential is 4.2 V, the discharge behavior of the cell is predicted. At the beginning of discharge, the negative electrode is fully lithiated while the positive electrode is ready to accept lithium ions. During discharge, the lithium

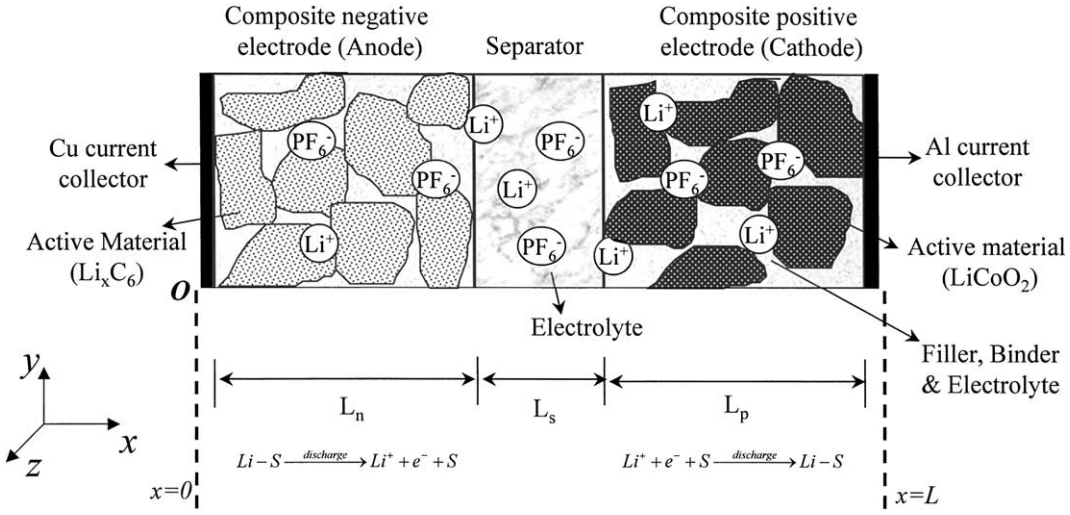

Fig. 1. A schematic of a typical Li-ion cell as well as a porous Ni–MH or Ni–Cd cell. In the case of nickel system replace $LiCoO_2$ with NiOOH, $LiPF_6$ with KOH, and Li_xC_6 with porous MH or Cd. $O \equiv (0\,0\,0)$.

ions deintercalate from the negative electrode particles and enter the solution phase, while in the positive electrode region lithium ions in the solution phase intercalate into the $LiCoO_2$ particles. This results in a concentration gradient, which drives lithium ions from the negative electrode to the positive electrode. The cell voltage decreases during discharge, as the equilibrium potentials of the two electrodes are strong functions of the concentrations of lithium on the surface of the electrode particles. The cell is considered to have reached the end of discharge when its voltage drops to 3.0 V. The kinetic, ohmic and mass transfer resistances result in heat generation inside the cell. This heat generation could be different at different points inside the cell. Thus, there develops a temperature distribution in all directions inside the cell, in addition to distributions in potentials and concentrations. A complete mathematical representation of such a system should include equations that describe: (1) mass transport of lithium in the solid phases, (2) mass transport of lithium ions in the solution phase, (3) charge transport in the solid phases, (4) charge transport in the solution phase and (5) energy transport in the whole cell.

1.3. Generalized model development

1.3.1. Assumptions

Listed below are some assumptions made to develop the model, the justification and usage of which in existing literature are cited alongside.

(a) The electrolyte (e.g. 1 M $LiPF_6$ in a 2:1 mixture of EC and EMC) is assumed to be binary with only Li^+ as the electroactive species [1,2].

(b) Side reactions are neglected.

(c) Butler–Volmer type kinetic expressions, of the form described below, are assumed to describe the charge transfer processes occurring across both the electrode/electrolyte interfaces. Thus, the divergence of the local solution phase current density at any point is given by [2]

$$\nabla i_2 = J = \begin{cases} a_j i_{0,j}\left[\exp\left(\dfrac{\alpha_{a,j}F}{RT}\eta_j\right) - \exp\left(-\dfrac{\alpha_{c,j}F}{RT}\eta_j\right)\right], & j = \text{n, p} \\ 0, & \text{otherwise} \end{cases} \quad (1)$$

In addition, the variation of current with solid and solution phase concentrations is accounted for by using a concentration-dependent exchange current density [1].

$$i_{0,j} = k_j (c_{1,j}^{\max} - c_{1,j}^{s})^{\alpha_{a,j}} (c_{1,j}^{s})^{\alpha_{c,j}} (c_2)^{\alpha_{c,j}}, \quad j = \text{n, p} \quad (2)$$

(d) The active material in each electrode is taken to be made of spherical particles of a single size, which enables one to represent mass transport inside the particle with a spherical diffusion equation. Further, the specific areas of the electrodes can be calculated from the equation

$$a_j = 3\frac{\varepsilon_{1,j}}{\delta_j}, \quad j = \text{n, p} \quad (3)$$

(e) The reversible part of the heat generated due to charge transfer reactions at the interfaces is neglected. This heat is proportional to the quantities $\partial\phi_{j,\text{ref}}/\partial T$, which

are not known for the $Li_xC_6/LiPF_6/Li_yCoO_2$ system and are expected to be small [8]. Therefore, the variations of $\phi_{j,\mathrm{ref}}$ with temperature are not considered, i.e. $\partial\phi_{j,\mathrm{ref}}/\partial T = 0$.

(f) Arrhenius type expressions are assumed to describe the temperature variations of kinetic and transport parameters [6].

$$P = P_{\mathrm{ref}} \exp\left[\frac{E_{\mathrm{a,p}}}{R}\left(\frac{1}{T_{\mathrm{ref}}} - \frac{1}{T}\right)\right],$$
$$P = i_{0,\mathrm{n}}, i_{0,\mathrm{p}}, D_{1,\mathrm{n}}, D_{1,\mathrm{p}}, D_2, \kappa \tag{4}$$

Other parameters like $\phi_{j,\mathrm{ref}}$, ρ, C_p, λ and σ are taken to be temperature invariant.

(g) Volume changes arising during cell operation are neglected resulting in constant electrode porosities [1].

(h) Constant values for transference number and solution phase diffusivity are assumed at all times and at all points in the cell.

1.3.2. Governing equations

Application of energy balance [6,7] around an arbitrary volume element inside the cell yields

$$\rho C_{\mathrm{p}} \frac{\partial T}{\partial t} = \nabla \cdot (\lambda \nabla T) + q \tag{5}$$

where the local source term is given by [6] (see assumption (i)),

$$q = \sigma \nabla\phi_1 \cdot \nabla\phi_1 + \kappa \nabla\phi_2 \cdot \nabla\phi_2 + \kappa_{\mathrm{D}} \cdot \nabla \ln c_2 \cdot \nabla\phi_2 + a_j i_j \left(\eta_j + T\frac{\partial \phi_{j,\mathrm{ref}}}{\partial T}\right), \quad j = \mathrm{n,p} \tag{6}$$

The first three terms arise from ohmic heating in the solid and solution phases. The last term is the heat generated due to charge transfer at the electrode/electrolyte interfaces. This involves a reversible part, proportional to $\partial\phi_{j,\mathrm{ref}}/\partial T$, and an irreversible part, proportional to η_j. Assumption (e) reduces the heat generation to

$$q = \sigma \nabla\phi_1 \cdot \nabla\phi_1 + \kappa \nabla\phi_2 \cdot \nabla\phi_2 + \kappa_{\mathrm{D}} \nabla \ln c_2 \cdot \nabla\phi_2 + a_j i_j \eta_j, \quad j = \mathrm{n,p} \tag{7}$$

where the surface overpotential, η_j, is defined to be

$$\eta_j = \phi_1 - \phi_2 - \phi_{j,\mathrm{ref}} - \frac{J}{a_j} R_{\mathrm{f},j}, \quad j = \mathrm{n,p} \tag{8}$$

The last term on the RHS denotes the loss due to a resistive film formed over the electrode particles. The value of the resistance of this film is not known and, therefore, it is used as an adjustable parameter. The equilibrium potentials $\phi_{j,\mathrm{ref}}$ are known to vary strongly with state of charge (SOC) and are expressed as functions of θ_j (also see assumption (f)) where

$$\theta_j = \frac{c_{1,j}^{\mathrm{s}}}{c_{1,j}^{\max}}, \quad j = \mathrm{n,p} \tag{10}$$

Expressions obtained from fitting the experimental data are used to represent the variation of $\phi_{j,\mathrm{ref}}$ with θ [1]. The last term in Eq. (8) is included in order to correct for film resistances at the electrode/electrolyte interfaces.

Applying Ohm's law for charge transport in the solid and solution phases after modifying it to account for concentrated solutions, one obtains the governing equations for potential distributions in the two phases [6].

$$\nabla \cdot (\sigma^{\mathrm{eff}} \nabla\phi_1) - J = 0 \tag{11a}$$

$$\nabla \cdot (\kappa^{\mathrm{eff}} \nabla\phi_2) + \nabla \cdot (\kappa_{\mathrm{D}} \nabla \ln c_2) + J = 0 \tag{11b}$$

where the effective conductivities are given by Bruggeman's correlation [1]

$$\kappa^{\mathrm{eff}} = \kappa \varepsilon_2^{\mathrm{brug}_j}, \quad j = \mathrm{n,s,p} \tag{12}$$

and

$$\sigma_j^{\mathrm{eff}} = \sigma_j \varepsilon_{1,j}^{\mathrm{brug}_j}, \quad j = \mathrm{n,p} \tag{13}$$

and the diffusional conductivity κ_{D} is given by [6]

$$\kappa_{\mathrm{D}} = \frac{2RT\kappa^{\mathrm{eff}}(t^+ - 1)}{F}\left[1 + \frac{\partial \ln f}{\partial \ln c_2}\right] \tag{14}$$

From assumption (h), the differential term vanishes from Eq. (14). Once again, the experimental data has been fitted to describe the variation of κ with concentration of electrolyte.

Species conservation on any electrode particle using assumption (d) results in the Eq. (1)

$$\frac{\partial c_{1,j}}{\partial t} = \frac{1}{r^2}\frac{\partial}{\partial r}\left[r^2 D_{1,j}\frac{\partial c_{1,j}}{\partial r}\right], \quad j = \mathrm{n,p} \tag{15}$$

and on the solution phase results in the equation after assumption (h)

$$\varepsilon_2 \frac{\partial c_2}{\partial t} = \nabla \cdot (D_2^{\mathrm{eff}} \nabla c_2) + \frac{(1 - t^+)}{F} J \tag{16}$$

The effective diffusivity is given by Bruggeman's correlation [1] as

$$D_2^{\mathrm{eff}} = D_2 \varepsilon_2^{\mathrm{brug}_j}, \quad j = n,s,p \tag{17}$$

1.3.3. Initial, boundary and interface conditions

Uniform initial conditions were used for T, c_1 and c_2

$$\text{at } t = 0, \quad T = T^0 \quad \text{for all } x,y,z \geq 0 \tag{18}$$

$$\text{at } t = 0, \quad c_{1,j} = c_{1,j}^0 \quad \text{for all } x,y,z \geq 0 \tag{19}$$

and

$$\text{at } t = 0, \quad c_2 = c_2^0 \quad \text{for all } x,y,z \geq 0 \tag{20}$$

At all boundaries, except the current collector/tab interfaces, flux boundary conditions are applied for the dependent variables. For temperature, the flux is equated to the heat lost to the surroundings according to Newton's law of

cooling. For the potentials and solution phase concentration, the respective fluxes are equated to zero. Mathematically,

$$-\lambda\frac{\partial T}{\partial m} = h(T - T_{\text{amb}}) \tag{21}$$

$$\frac{\partial \phi_1}{\partial m} = 0 \tag{22}$$

$$\kappa\frac{\partial \phi_2}{\partial m} + \kappa_{\text{D}}\frac{\partial \ln c_2}{\partial m} = 0 \tag{23}$$

$$\frac{\partial c_2}{\partial m} = 0 \tag{24}$$

where m denotes the outward normal to the boundary. The boundary condition for ϕ_1 changes at the tab/current collector interfaces. On the copper current collector/tab interface, ϕ_1 is arbitrarily set to 0, while on the aluminum current collector/tab interface, the matrix phase current density is equated to the applied current density, i.e.

$$-\sigma_j^{\text{eff}}\frac{\partial \phi_1}{\partial m} = i_{\text{app}}, \quad j = \text{n, p} \tag{25}$$

For diffusion inside the electrode particles [1]

$$\text{at } r = 0, \quad \frac{\partial c_{1,j}}{\partial r} = 0, \quad j = \text{n, p} \tag{26}$$

$$\text{at } r = \delta_j, \quad -D_{1,j}\frac{\partial c_{1,j}}{\partial r} = \frac{J}{a_j F}, \quad j = \text{n, p} \tag{27}$$

At the interfaces between the different regions in the cell, the following conditions are applied to maintain the continuity of fluxes. At all interfaces, all fluxes on the left of the interfaces are equated to those on the right [8]. The exceptions are

$$\text{at } x = L_{\text{Cu,n}}, \quad \begin{cases} \kappa^{\text{eff}}\dfrac{\partial \phi_2}{\partial x}\bigg|_+ + \kappa_{\text{D}}^{\text{eff}}\dfrac{\partial \ln c_2}{\partial x}\bigg|_+ = 0 \\ \dfrac{\partial c_2}{\partial x}\bigg|_+ = 0 \end{cases} \tag{28}$$

$$\text{at } x = L_{\text{n,s}}, \quad \frac{\partial \phi_1}{\partial x}\bigg|_- = 0 \tag{29}$$

$$\text{at } x = L_{\text{s,p}}, \quad \frac{\partial \phi_1}{\partial x}\bigg|_+ = 0 \tag{30}$$

$$\text{at } x = L_{\text{p,Al}}, \quad \begin{cases} \kappa^{\text{eff}}\dfrac{\partial \phi_2}{\partial x}\bigg|_- + \kappa_{\text{D}}^{\text{eff}}\dfrac{\partial \ln c_2}{\partial x}\bigg|_- = 0 \\ \dfrac{\partial c_2}{\partial x}\bigg|_- = 0 \end{cases} \tag{31}$$

1.4. Full cell isothermal models

Doyle et al. [3] validated their isothermal model by comparing it with the experimental data obtained from Bellcore (presently Telcordia Inc.) plastic Li-ion (PLION) cells [3]. Using D_2, D_1, R_{f}, t^+ and brug as adjustable parameters, they could obtain good agreement for low and moderate rates. However, in a later communication, Arora et al. [9] showed that the simulations based on the same model do not agree with the experimental data at higher rates. They attributed this mismatch to one or more of the following assumptions involved in the model:

(i) no salt precipitation;
(ii) no solvent transport or segregation of the two solvents;
(iii) constant solid and solution phase transport properties.

They investigate the reasons one after another in view of relaxing them to obtain better fits to experimental data.

Salt precipitation may occur in the negative electrode region during discharge if the local concentration of the electrolyte reaches values above its solubility limit. For the discharge rates considered in their work, they showed that the electrolyte never reaches saturation and, consequently, they discarded the idea of including salt precipitation effects in their model. The authors, however, deemed solvent segregation as highly possible when current is passed through a mixture of solvents. Further, the polymer electrolyte matrix used in PLION cells was treated to be an inert binder, which might, in reality, interact with the ionic species. To include these effects, mass transport in the solution had to be described considering the electrolyte as being multi-component in nature as opposed to binary. Such a treatment of the electrolyte would require knowledge of 10 independent transport properties for the five species involved (the polymer, the two solvents, Li^+ and PF_6^-). Due to lack of available data, this approach was also discarded.

For the rates (1.5–3C) considered in their work, the authors show that it is predominantly the solution phase diffusion that limits cell performance. Therefore, it was clear that the value of D_2 used in the simulation is very critical in predicting the experimental data. Further, the fact that the local solution phase concentration varied significantly with position inside the cell at high rates suggested that using a concentration-dependent D_2 would result in better fits. But since no experimental data was available relating D_2 with c_2, the authors tried various algebraic expressions of the form: (i) $D_2 = D_2^0 + m(1 - c_2)$, (ii) $D_2 = D_2^0 \exp(mc_2)$, (iii) $D_2 = mf(\kappa)$ where $\kappa = f(c_2)$, etc. They used each of the mentioned expressions in the simulations but found that none of them could predict the experimental data any better without the use of other adjustable parameters. However, by using a rate-dependent D_2 they could fit all discharge rates well. The values of D_2 used for three different cells (called thin, medium and thick based on the thickness of the electrodes used) are shown as a function of discharge rate in Fig. 2. The authors acknowledge that this makes the model empirical and, therefore, usable only within the range of discharge rates considered in their work. For rates as high as 3C, solid phase diffusion limitations were shown to

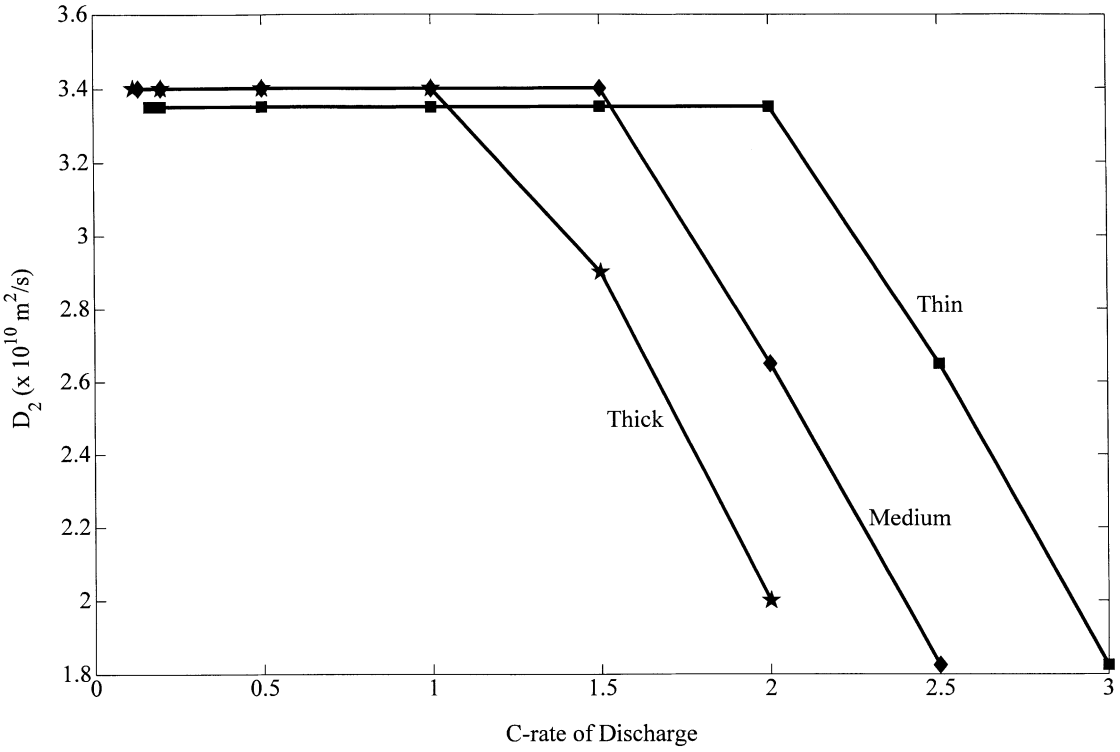

Fig. 2. Solution phase diffusion coefficient as a function of discharge rate used to fit experimental data for three different cells. 1*C* corresponds to 1.156, 1.937 and 2.691 A/m^2 for thin, medium and thick cells, respectively.

become important and the value of D_p was also varied with rate to obtain good fits to experimental data.

The aforementioned method of varying D_2 as a function of rate was also employed by Gomadam et al. [10] in order to obtain good fits to experimental data for constant current discharges over a very wide range of rates ((1/5)–10*C*). However, unlike Arora et al. [9], Gomadam et al. [10] found that the value of D_2 had to be increased with discharge rate. Using the relation between D_2 and i_{app} from constant current discharges, they simulated pulse discharges for different amplitudes (peak currents), duty cycles and frequencies. The simulated cell voltage plotted as a function of discharge capacity in Fig. 3, compared well with the experimental data. The value of D_2 during the intermittent rest periods of a pulse discharge was used as an adjustable parameter to obtain good fits to experimentally obtained data for voltage relaxation of the cell with time. It should be noted that the authors assumed very fast transport of lithium in the solid phase at all rates.

Guo et al. [11] developed a model to estimate the solid phase diffusion coefficient from experimental impedance data. Their model followed the model of Doyle et al. [12] for impedance response of a Li-ion system. Using this full cell model Guo et al. [11] simulated the impedance response of a Li-ion cell as shown in Fig. 4. Also shown in Fig. 4 are the impedance responses of the individual cell components. Treating these as experimental data, the authors described a method, called the modified EIS method, to extract the solid phase diffusion coefficient by the technique of non-linear parameter estimation. They concluded that the validity of estimating the diffusion coefficient from the impedance response of a porous intercalation electrode by the modified EIS method is not assured if the transport of lithium ions in the solution phase is limiting cell performance. They identified the ratio of the time constants of solid and solution phase diffusions as a dimensionless parameter governing the reliability of the estimation of the solid phase diffusion coefficient. Their results showed that bigger particle sizes, smaller electrode thicknesses, larger differences in the values of the solid and solution phase diffusion time constants and small active material loading are more conducive to a valid estimation of the solid phase diffusion coefficient.

The model developed by Doyle et al. [1] for isothermal constant current discharge of Li-ion cells was extended by Arora et al. [13] to include the lithium deposition side reaction occurring during overcharge conditions. They proposed a simple mechanism of $Li^+ + e^- \rightarrow Li$ for the reduction of lithium ions on parts of the carbon electrode where the potential reaches 0 V with respect to a Li/Li$^+$ reference electrode. The total local reaction rate (J) in the negative electrode was calculated as the sum of two individual reaction rates: (1) the rate of the desired lithium intercalation reaction ($J_{n,1}$) and (2) the rate of deposition of lithium metal ($J_{n,2}$).

$$j_n = a_n \sum_{k=1}^{2} i_{0,k}[\exp(\alpha_{a,k} f\eta_k) - \exp(-\alpha_{c,k} f\eta_k)] \quad (32)$$

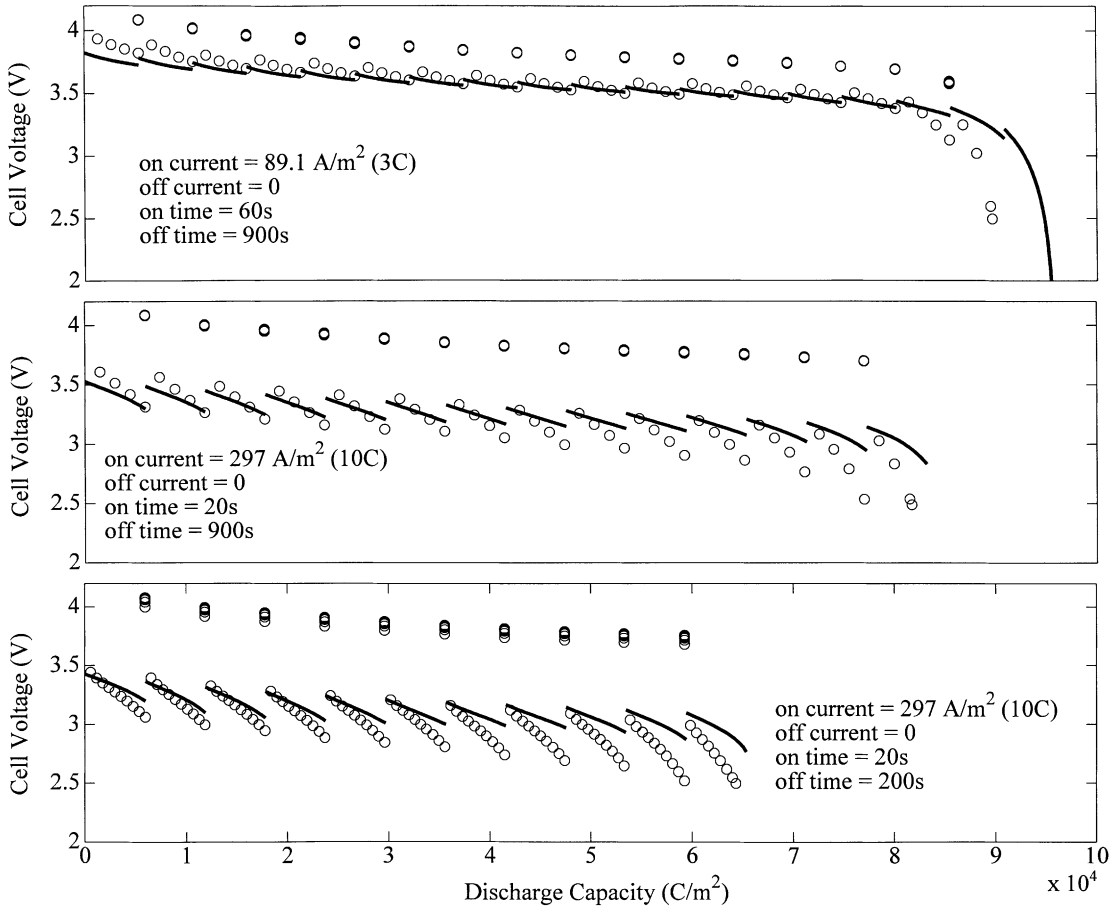

Fig. 3. Comparison of simulated voltage profiles with experimental data for pulse discharge. The solid lines denote model predictions while the circles denote the experimental data.

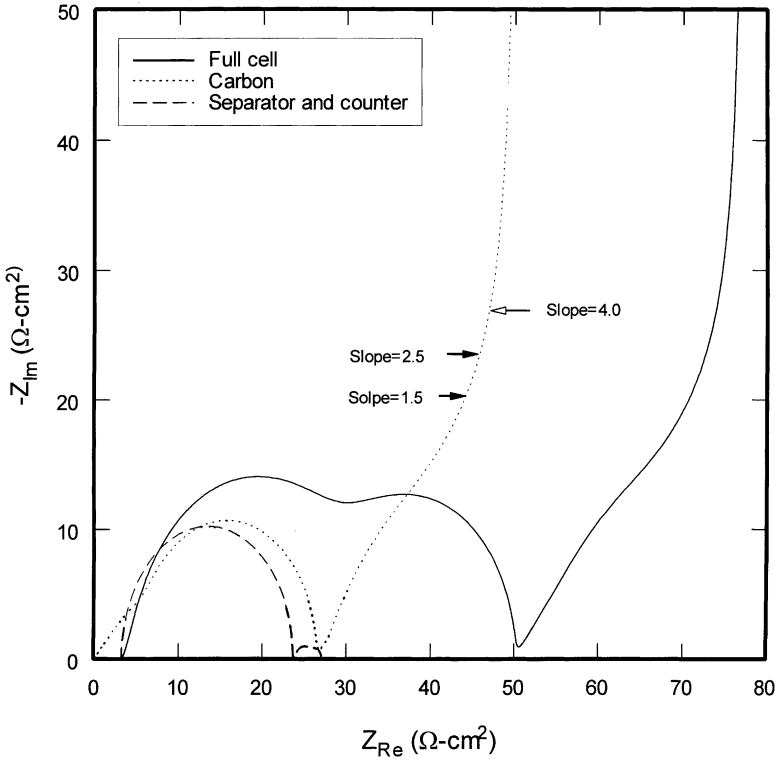

Fig. 4. Simulated impedance responses of a full cell and its components.

where $i_{0,1}$ is defined by Eq. (2) and

$$i_{0,2} = k_2 c_2^{\alpha_{a,2}} \tag{33}$$

The authors study the effect of lithium deposition on charge efficiency and capacity fade. Further, they use the model to optimize certain design parameters (like negative electrode thickness, particle size and excess capacity) and operating conditions (like charging rate and charge cut-off voltage). They found that a cell with 5% excess negative electrode when charged to 4.25 V at 1*C* rate will lead to lithium deposition, which occurs after the cell crosses 4.2 V. Further, if the same cell had 19% excess capacity in the negative electrode, no lithium deposition would be observed even if the cell was overcharged to 4.45 V at 1*C* rate. However, at higher rates, a small amount of lithium deposition will be observed when the cell is overcharged to 4.45 V. Thus, the authors conclude that the lithium deposition side reaction can be reduced significantly by using excess negative electrode capacity, although the downside being the resulting enhanced first cycle capacity loss.

The authors also found that active material particle size and electrode thickness also affect lithium deposition. Thinner electrodes with smaller particle sizes were found to be less prone to lithium deposition than thicker electrodes with larger particles. The lithium metal deposited on the negative electrode was also considered to react irreversibly with the solvent forming a film of insoluble products (e.g. Li_2CO_3) around the active material particles. This resulted in an increase in the cell resistance, which was shown to affect the cell capacity loss depending on its composition. The resistance offered by this film to current flow was calculated as

$$R_{\text{film}} = R_{\text{f,n}} + \chi_{\text{Li}}\left(\frac{\delta_{\text{film}}}{\kappa_{\text{Li}}}\right) + \chi_{\text{Li}_2\text{CO}_3}\left(\frac{\delta_{\text{film}}}{\kappa_{\text{Li}_2\text{CO}_3}}\right) \tag{34}$$

where the film thickness δ_{film} is given by

$$\frac{\partial \delta_{\text{film}}}{\partial t} = \frac{J_{\text{n},2} M}{a_{\text{n}} \rho F} \tag{35}$$

The resistance offered by the film was found to increase with an increase in Li_2CO_3 composition resulting in earlier end of discharge and, consequently, loss of discharge capacity.

The models discussed thus far and those discussed in the subsequent sections, assume that the electrodes consist of active material particles of one size. However, in reality, electrodes contain particles of a range of sizes. In order to understand the effect of multiple-sized particles on the performance of the cell, Nagarajan and Van Zee [14] developed a model assuming that the cathode consisted of particles of two different sizes. They used the dilute solution theory to describe species transport in the solution phase. Based on the linear packaging model developed by Yu et al. [15], they accounted for the porosity of the electrode as a function of the mixture of particles of different sizes. The authors considered a binary mixture of small and large particles, where the volume fractions of the small (χ_{S}) and large (χ_{L}) particles are known. The specific volume of the mixture is calculated based on the volume fractions of the particles and the specific volume for a random packing of spheres (v). The equation for the specific volume will depend on the array matrix

$$v_{\text{L}} = v\chi_{\text{L}} + v_{\text{S}}\chi_{\text{S}} \tag{36}$$

$$v_{\text{S}} = v\chi_{\text{S}} + v_{\text{L}}\chi_{\text{L}} \tag{37}$$

Eq. (36) applies for a matrix of large particles where the voids are filled with small particles, while Eq. (37) applies for a matrix of small particles where the voids are filled with large particles. The specific volume of the mixture of particles is given by the maximum between v_{S} and v_{L}. The maximum was chosen to avoid overlapping of the particles. The other equations used to complete their model are given as Eqs. (23), (24), (26) and (27) in their paper [14]. They concluded that a binary mixture can provide a significantly higher density of active material relative to an electrode comprised of single size particles. However, increasing the packing density increases the liquid phase diffusion resistance, and therefore, there must be an optimum size ratio for these variables that maximizes the capacity of the cell.

1.5. Full cell non-isothermal models

Pals and Newman [4] included an energy balance in the isothermal model developed by Doyle et al. [1] in order to describe non-isothermal conditions in single Li-ion cells and batteries (sets of single cells). However, they used a lumped heat generation term, based on the difference between the equilibrium cell voltage and the actual cell voltage, to calculate the temperature.

$$q = \frac{V_{\text{eq}} - V - T(\text{d}V_{\text{eq}}/\text{d}T)}{L_{\text{cell}}} i_{\text{app}} \tag{38}$$

Elsewhere, Rao and Newman [16] showed that this method of calculating the heat generation term is accurate only under conditions of uniform reactions distribution (e.g. low rate discharges). Extending the single cell thermal model developed by Pals and Newman [4], Botte et al. [8] included a chemical side reaction (the negative electrode decomposition), which being an additional source of heat resulted in enhanced temperature rise in the cells.

$$q = \frac{V_{\text{eq}} - V - T(\text{d}V_{\text{eq}}/\text{d}T)}{L_{\text{cell}}} i_{\text{app}} - \Delta H_{\text{rxn}} R \tag{39}$$

In the absence of such side reactions, the cell temperature would increase only due to the irreversible heat generated by electrochemical charge and mass transport and once the cell temperature reaches the melting point of the separator the cell would shut down. No further heat will be generated and, therefore, the cell temperature would not rise above the melting point of the separator. On the other hand, if there

were chemical side reactions occurring inside the cell, the cell temperature would continue to rise beyond the melting point of the separator. The final temperature attained by the cell has been shown by Botte et al. [8] to be sensitive to the reaction parameters namely E_a and ΔH_{rxn}. They also studied the effect of some design and operating parameters on the temperature attained by the cell in the absence of any side reactions. The heat transfer coefficient has been pointed out to be a very important parameter that determines the heat generated in the cell. Starting from the ambient temperature of 25 °C, the authors show that, for a 3*C* discharge, the cell temperature reaches values as high as 90 °C when h is 0 W/(m^2 K) as opposed to 45 °C when h is 20 W/(m^2 K). They also show that the final cell temperature increases from 30 to 80 °C when the rate of discharge is increased from 1/2 to 3*C* with a heat transfer coefficient of 5 W/(m^2 K). Further, when the capacity of the cell is increased by increasing the electrode thicknesses, the final temperature attained by the cell increases for a given *C*-rate discharge. They also studied the effect of electrode particle size on the temperature attained by the cell. They found that a cell with 30 μm particles reached 60 °C, while that with 10 μm particles reached only 40 °C during the 1*C* discharge.

Following Wang et al. [6], Gomadam et al. [7] modified the electrochemical-thermal model developed by Pals and Newman [4] by calculating heat generation locally instead of using a lumped method (see Eq. (6)). They established the validity of this method by comparing (see Fig. 5) the single cell model predictions with experimental data obtained from cylindrical 18650 cells. The voltage–time predictions of the model agreed well with experimental data both quantitatively and qualitatively. The temperature–time predictions, however, agreed only qualitatively well and showed some quantitative mismatches. The authors attributed this to errors in estimation of unknown parameter values and/or violation of one or more of their assumptions (e.g. entropies are negligible). The authors also extend the model to two dimensions in order to capture non-uniformities along the height of the cell. They show that these effects are important particularly when the height of the cell is much larger than its thickness. The final temperatures attained by the top and bottom of the cell was found to first increase with discharge rate and then decrease with further increase in the discharge rate. This is explained based on the fact that the temperature attained by the cell is proportional to the product of the rate of heat generation (q) and the discharge time (t_D). Since q increases and t_D decreases with increase in discharge rate, their product goes through a maximum and the cell temperature follows suit. The authors also conducted some case studies that produced counter-intuitive results, which could be predicted only by calculating the heat generation term locally. A cell in which current enters and leaves only through the tabs connected to the top of the current collector was considered to lose heat to the ambiance only through its bottom face, characterized by a heat transfer coefficient (h). In such a case, one would expect the cell temperature to decrease at all points when the value of heat transfer coefficient is increased. The model, however, predicts that the temperature at the top portion of the cell would increase while that at the bottom part would decrease as expected. This effect has been explained based on a non-uniform distribution of heat generation (q) inside the cell. For non-zero values of h, as discharge proceeds, the bottom part of the cell loses heat and hence becomes more resistive while the top part becomes hotter and more conductive. This makes the current distribution and, consequently, the heat generation even more non-uniform. More current flows through the top and thus the top part gets progressively hotter. The increase in the local solution phase current (i_2) near the top part of the separator with time and the corresponding decrease in i_2 near the bottom part are shown in Fig. 6 for a cell 419 μm thick and 1 m tall. The authors emphasize that the lumped heat generation method used by Pals and Newman [4] or the method used by Song and Evans [5] cannot predict such results. Further, they extend the two-dimensional (2D) single cell model to a battery (a set of single cells) using the modified heat generation method explained by Pals and Newman [4]. The advantage of this method is that the electrochemical-thermal model has to be solved only sequentially as opposed to simultaneously in the rigorous way.

In the models discussed earlier, the intercalation of lithium into the solid electrode particles was described by a spherical diffusion equation characterized by a constant diffusion coefficient. However, it has been shown that the diffusion of lithium inside the electrode particles is non-ideal and does not obey Fick's law of diffusion. In order to accurately describe the transport of lithium through the solid, one has to correct the diffusion coefficient by an activity term. Verbrugge and Koch [17] developed a theoretical approach to calculate this activity term for carbon fiber electrodes from experimentally measured equilibrium potential data. Following them, Botte and White [18] showed the importance of using such an activity corrected diffusion coefficient over the constant diffusion coefficient when simulating constant current discharges. For this study, they considered a cell made of a lithium metal cathode and a porous carbon fiber anode, which are the same as that considered by Verbrugge and Koch [17]. Following the model developed by Doyle et al. [1] for constant current discharges, Botte and White [18] showed that for low discharge rates, when solid phase diffusion, as well as other transport processes do not limit the cell performance, the two methods predicted identical results. However, for high rates, the constant diffusion coefficient method could predict voltages up to 0.25 V lower than those predicted using the corrected diffusion coefficient method. Further, the constant diffusion method predicted an earlier end of discharge. The authors also compared the cell temperatures as a function of time and discharge rate. At low rates, the two methods predicted exactly the same temperature profiles while at higher rates, the cell temperature as predicted by the

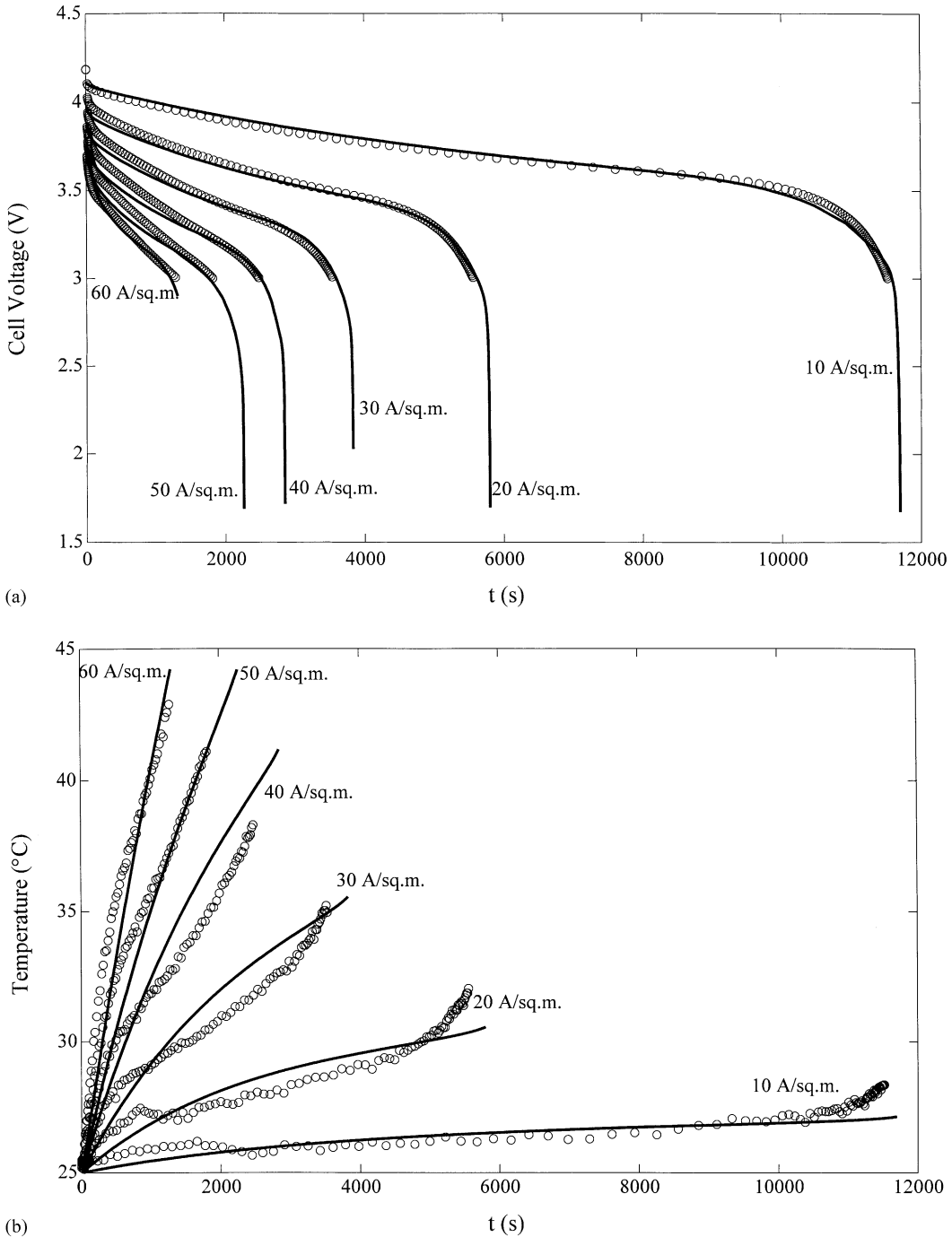

Fig. 5. Comparison between (a) the *V–t* and (b) the *T–t* curves obtained for different discharge rates from experiment and those predicted by the model. The solid lines denote model predictions while the circles denote the experimental data (reproduced from [7] by permission of The Electrochemical Society).

constant diffusion method increased more steeply with time. However, the final temperature attained by the cell was higher in the case of the corrected diffusion method since discharge lasted longer. They also report significant mismatches between the two methods with regard to the concentration profiles inside the solid particles. As a result of the aforementioned observations, the authors conclude that the corrected diffusion coefficient method must be preferred over the constant diffusion coefficient method especially at high discharge rates.

1.6. Single particle models

Zhang et al. [19] developed a spherical diffusion model to predict the potentiodynamic response of a single spinel particle. Assuming a constant solid phase diffusion coefficient

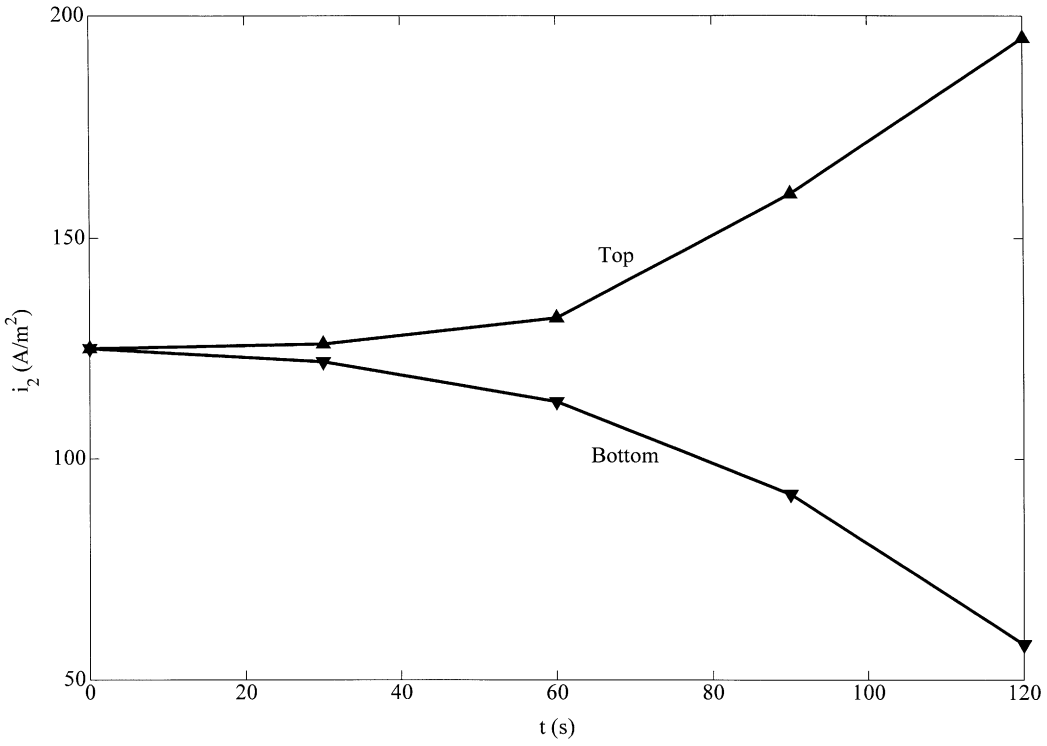

Fig. 6. Time evolution of the local solution phase current density in the separator at the top and bottom of the cell. $h = 10^4$ W/(m^2 K), $L = 419$ μm, $I_{app} = 125$ A/m^2, $H = 1$ m, $T^0 = 298$ K, $T_{amb} = 0$ K.

(D_1) and using that as an adjustable parameter along with the rate constant (k), they simulated cyclic voltammetry experiments conducted by Uchida et al. [20]. Four distinct peaks were observed with two each on the anodic and cathodic scans. Comparison between the experimental data and the model predict ions yielded values of 2.2×10^{-9} cm^2/s and 0.00019 cm$^{5/2}$/(mol$^{1/2}$ s) for D_1 and k, respectively. Zhang et al. [19] also studied the effect of parameters like scan rate on the predicted cyclic voltammogram. They observed that when the scan rate is increased, the height of all the peaks increased. Further, the potentials at which the anodic peaks occurred shifted to more positive values while the cathodic peaks shifted to more negative values. The height of the first peak varied linearly with the square root of scan rate and the relationship was shown to agree well with literature values. The other peaks, however, could not be related linearly to the square root of scan rate and this has also been reported by previous researchers. Zhang et al. [19] grouped the rate of electrochemical reaction and the rate of lithium diffusion into a single dimensionless parameter b given by

$$b = \frac{krc_2^{1-\alpha}}{D_1} \tag{40}$$

Keeping the value of D_1 constant, the effect of varying b was studied. Initially, the peak current increased strongly with b but after a point the peak height became insensitive to b. Based on this observation the authors concluded that for low values of b both kinetic and diffusion limitations were important and, therefore, the peak current increased with b. But as b kept increasing, a point was reached when kinetics became too fast and the system was entirely diffusion limited. As a result, a further increase in b did not increase the peak current. The authors also studied the effect of the anodic transfer coefficient (α_a) on the simulated cyclic voltammogram. They observed that for high values of b, α_a had no effect on the cyclic voltammogram while for low values of b, a decrease in α_a favored the anodic reaction more and made the values of peak potentials smaller. This is because when b is low, kinetics is slow and consequently a decrease in α_a has an effect on the peak potential. On the other hand, when kinetics is fast, i.e. when b is high, change in α_a does not produce any effect on the voltammogram.

The models developed by Doyle et al. [1], and later extended by Pals and Newman [4], Arora et al. [10,13] and Botte et al. [8], were mathematically 2D with x being the dimension across the cell thickness and r being the dimension along the radii of the spherical active material particles in the electrodes. Since r does not represent a physically new dimension, it is often referred to as a pseudo-dimension and the corresponding models as pseudo-2D models. In solving these models Doyle et al. [1] and Arora et al. [10,13] used a technique called Duhamel's super-position to collapse the pseudo-dimension r, thereby making the model 1D. By this method, one can express the surface concentration on the electrode particle directly as an infinite series in D_1t/r^2. One disadvantage of this method is that in order to obtain accurate results a large number of algebraic calculations have to be made at each node point in x for each time

step. This calculation can be reduced significantly by using the method suggested by Subramanian and White [21] when solving for diffusion in the solid phase. In their method, a solution for local concentration (c_1) as a function of r and t is assumed to be of the form

$$c_1 = \sum_{i=0}^{N} A_i(t) r^{2i} \tag{41}$$

where the number of terms (N) depends on the accuracy required. The coefficients $A_i(t)$ are found by forcing the solution to satisfy the boundary conditions, as well as the governing equation at conveniently selected points in r. The number of parameters $A_i(t)$ to be determined is exactly the same as N and, therefore, the corresponding model is called the N-parameter model. Subramanian and White [21] conduct case studies for three different values of N, namely, 2, 3 and 4. As a result of comparison the exact solution with the two-, three- and four-parameter models for constant current discharges, the authors conclude that the four-parameter model predicts solutions with good accuracy even for high discharge rates (say 10C). The two- and three-parameter models, however, make significantly erroneous predictions at such high rates and must be used with caution even at moderate rates. At low rates, all the three models predict results that match very well with the exact solution. This method was used in a full cell model by Gomadam et al. [7] in solving for lithium transport in the active material solid particles.

1.7. Conclusions

A review of the modeling efforts of researchers in the field of Li/Li-ion batteries at the University of South Carolina is presented. The review included models that describe the behavior of single electrode particles, single electrodes and full cells under various operating conditions like cyclic voltammetry, constant current discharge and impedance. It was concluded that the models presented must be extended to include several phenomena like concentration dependencies of diffusion coefficients, state of charge dependencies of half cell entropies and salt precipitation at high discharge rates. Efforts are currently underway at the University of South Carolina to understand these phenomena so as to enable our models to predict reality closer.

2. Modeling of nickel based batteries

2.1. Background

The nickel hydroxide electrode has proved to be one of the most enduring battery chemistries, with widespread use in a variety of applications ranging from portable electronics to satellites. Used in a number of battery systems, including the nickel–cadmium, nickel–metal hydride, nickel–zinc and nickel–hydrogen, the chemistry in the nickel hydroxide electrode has proved sufficiently pliable to suit many an application. Present interest stems from use in space applications, including in the Hubble space telescope (Ni–H_2) [22] and for use in electric cars (Ni–MH) [23]. The original patent for the nickel–cadmium cell can be traced back to the last decade of the 19th century and is attributed to a Swedish scientist, Junger [24] (cited by Salkind [25]). Its first commercial use in a large scale was reported in 1917, when it was used to light subway trains in Paris [26]. Since then, the advantages of the battery chemistry (e.g. cycle life, shelf life etc.) has ensured its dominance of the secondary battery market [27].

However, a century of research and development into this chemistry has not resulted in a fail-safe method of fabricating cells. Part of the problem stems from the complex nature of the nickel hydroxide redox behavior and the close relationship between the structure of the material and its electrochemical characteristics [28]. In addition, the miniaturization of most modern devices has thrown up new challenges in the field of design of batteries. Therefore, one is confronted with not only understanding the various physio-chemical processes that occur in battery systems, but also in designing them to suit our ever increasing demands. Mathematical models derived from continuum mechanics provide an effective tool for achieving both these ends. With the development of modern computers with enhanced speed, enormous opportunities are available for the development of robust theoretical descriptions of complex systems. In this paper, we detail the efforts that have been undertaken to model the nickel hydroxide active material over the last two decades. The purpose of the review is two-fold namely: (i) to give the reader an understanding of the theoretical basis for the various electrochemical signatures observed in the nickel electrode and (ii) to detail the efforts in developing design tools that relate various electrode properties (e.g. thickness, porosity) to the performance.

2.2. System description

Fig. 1 schematizes a cross-section of a cell constructed with the nickel positive electrode. The negative electrode used in the cell could be a porous electrode (Cd, MH) or a planar electrode (H_2). The nickel hydroxide active material is supported on a conductive matrix with the active material either pasted or impregnated into the pores of the sinter. There is considerable void volume in the electrode, which is flooded with electrolyte, typically concentrated KOH in the concentration range of 26–33% [29]. The electrodes represented in the figure can be thought of as half the actual electrode thickness, with equivalent processes occurring in the other half. Symmetry enables us to neglect the processes in the other half. The main reaction that occurs at the nickel electrode can be ideally represented as [30]

$$\mathrm{Ni(OH)_2 + OH^- \underset{\text{discharge}}{\overset{\text{charge}}{\rightleftarrows}} NiOOH + H_2O + e^-},$$
$$E_0 = 0.311\ \mathrm{V\ versus\ Ag/AgCl} \tag{42}$$

A proton and electron are released at the nickel site within the solid active material. The electron travels to the conducting substrate and eventually out to the external circuit. The proton diffuses through the active material to the solid/electrolyte interface where it combines with the hydroxyl ion to form water. On discharge, these processes are reversed.

On both charge and discharge, oxygen evolution occurs simultaneously with reaction 1, as the equilibrium potential of this reaction is more negative.

$$4OH^- \rightarrow O_2 + 2H_2O + 4e^-,$$
$$E_0 = 0.22\,\text{V versus Ag/AgCl} \quad (43)$$

In a sealed cell, the oxygen evolved in the positive electrode migrates to the negative electrode and is reduced (reverse of reaction (43)), thus ensuring that no excessive pressure builds up in the cell. The oxygen transfer in the cell is facilitated by using an oxygen permeable membrane and operating the cell under starved conditions, i.e. with limited amount of electrolyte.

Again, reaction (42) is a simplistic representation of the redox processes that occur in the electrode, as the active material is known to consist of different phases. Bode et al. [30] summarized the complex chemical and electrochemical processes as follows.

$$\begin{array}{ccc} \alpha - Ni(OH)_2 & \underset{\text{discharge}}{\overset{\text{charge}}{\rightleftharpoons}} & \gamma - NiOOH \\ \text{Dehydration}\ \downarrow & & \uparrow\ \text{Overcharge} \\ \beta - Ni(OH)_2 & \underset{\text{discharge}}{\overset{\text{charge}}{\rightleftharpoons}} & \beta - NiOOH \end{array} \quad (44)$$

Note that these reactions are not written as balanced reactions, but rather to illustrate the relationship between the various phases. The hydrated, non-close-packed phase, termed α-$Ni(OH)_2$, is unstable and dehydrates to the anhydrous close-packed phase, termed β-$Ni(OH)_2$, in concentrated alkali solution. Oxidation of β-$Ni(OH)_2$ results in the formation of β-NiOOH while oxidation of α-$Ni(OH)_2$ results in γ-NiOOH. The β-phase converts to the γ-phase on overcharge, as Ni(III) is converted to Ni(IV). Loyselle et al. [62] used a point defect approach to modify this reaction mechamism.

2.3. Cell models

In order to predict the performance of a nickel battery for a wide range of designs and operating conditions, a number of processes must be accounted for in terms of measurable parameters: (i) thermodynamics and kinetics of all redox reactions; (ii) transport of ions through all ionically conducting phases; (iii) the potential variations in both ionically and electronically conducting phases. The high concentration of OH^- in the cell (31%) necessitates the use of concentrated solution theory [31–35], where the interactions of the ions with the solvent also need to be considered. The complications introduced by the presence of the porous matrix are handled using porous electrode theory [34,36–38].

Macroscopic, porous electrode models have been developed for the nickel batteries [39–44] in order to understand how the complex interactions that occur among the anode, cathode and separator affect battery performance. For example, Micka and Rousar [39,40] developed a 1D model, but they noticed that on discharge the voltage curves could not be fitted adequately using normal Nernstian thermodynamics, especially at high states of charge. Fan and White [43] improved the predictions of the Ni–Cd discharge curves by using activity coefficient corrections to the Nernst equation, as suggested by Barnard et al. [45]. However, their model was unable to adequately predict the percent utilization of the active material on discharge as a function of current. This limitation resulted from assuming that the nickel hydroxide active material charged and discharged uniformly.

De Vidts and White [46] modeled a sealed Ni–Cd cell that includes proton diffusion and ohmic drop through the active material in the nickel electrode. The model was used to calculate the sensitivity coefficients for various parameters in the model. These calculations showed that the discharge voltage of the cell is affected mostly by the kinetics of the nickel reaction. Towards the end of discharge, proton diffusion was also found to become important, because the proton diffusion process affects the active material utilization significantly. During charge, the cell voltage is mainly affected by the kinetics of the nickel reaction until the oxygen evolution reaction begins, after which time the kinetics of the oxygen evolution has the largest effect. The oxygen evolution reaction is also the most influencing factor on the actual charge uptake of the cell by the end of a charge operation (charge efficiency). Compared with the rates of reaction and proton diffusion, the ohmic drop in the active material of the nickel electrode and the mass transport and ohmic drop in the electrolyte have negligible effect on the behavior of the cell studied here.

De Vidts et al. [47] also developed a model for predicting the discharge behavior of metal hydride electrode. The model was used to study the effect of various parameters on predicted discharge curves. The simulations obtained using the model show the expected decrease of charge utilization as the rate of discharge is increased. Increasing the particle size of the alloy and decreasing the diffusion coefficient of the hydrogen atoms in the hydride showed a similar effect on the discharge curves. The model simulations also show the critical role that the kinetic and transport parameters play in determining the overall shape of the predicted discharge curves for a metal-hydride electrode.

Mao and White [48] used a mathematical model to characterize the self-discharge of a NiOOH electrode in a hydrogen environment. The model included diffusion of

dissolved hydrogen in an electrolyte film, which covers a flooded electrode, electrochemical oxidation of hydrogen, reduction of NiOOH, and changes of surface area and porosity of the electrode during the self-discharge process. Although the self-discharge process is complicated, the predictions of the model are consistent with experimental results reported in the literature, which include linear relationships between the logarithm of hydrogen pressure and time and between the logarithm of the capacity remaining and time. The model predictions indicate that hydrogen oxidation takes place predominantly near the front side of the electrode, but the reduction of NiOOH takes place uniformly throughout the electrode.

Mao et al. [49] improved the percent utilization predictions of Barnard et al. [45] by adding the diffusional resistance of protons to their pseudo 2D model. However, this model is unable to predict the change in performance of the battery on cycling because the redox reaction in the active material is assumed to be the overly simplistic reaction (1). Adding a more sophisticated reaction mechanism to the model is required in order to predict performance during cycling.

During the discharge of nickel hydroxide electrodes, two voltage plateaus have been frequently observed [29,50]. While the first plateau occurs due to the nickel oxidation/reduction reaction via reaction (42), the second plateau appears approximately 400 mV cathodic of it and has been reported to have as much as 50% of the capacity of the first plateau [29]. Mao et al. [49] modeled the second discharge plateau in a nickel–hydrogen cell using a comprehensive cell model, which incorporates proton diffusion and porous electrode theory using a pseudo 2D approach. They considered the conductivity of the active material to be a continuous function until a state of change of 0.1. At this point, the authors assumed a discontinuity in the conductivity at a constant low value. This can be interpreted as a model that incorporates the first explanation of the second plateau given where the conductivity of the active material decreases steadily during discharge between the state of charge of 1 and 0.1. At this low state of charge the conduction in the film shifts from electron conducting to hole conducting and the hole conductivity is a constant at around $1.2 \times 10^{-8}/(\Omega\,\mathrm{cm})$. This low conductivity results in a greater ohmic drop and hence the potential where the reaction occurs is lower.

In contrast to the models that assume the conductivity to be the cause for the second discharge plateau, the model by De Vidts et al. [51] was successful in predicting the second discharge plateau for a Ni–H_2 cell by considering the oxygen reduction reaction (reverse of reaction (43)). Although, the oxygen reduction reaction has been included in previous models for the Ni–Cd battery developed by the authors [42–44,52] they do not predict the second plateau. The authors explain this by suggesting that the oxygen generated in the positive electrode in a Ni–Cd cell is transported to the negative electrode easily as the mass transfer resistance is low. At the negative electrode, the oxygen is reduced. Hence, not much dissolved oxygen is present in these cells. However, in a Ni–H_2 cell, the model predicts that there is ample oxygen present to sustain the reaction, which appears to be due to the gas phase present. De Vidts et al. [51] simulated the effect of oxygen pressure on the second discharge plateau and predict a change in potential to less negative values on increasing the pressure. In addition, the models predict that an increase the pressure would result in a bigger second plateau, as there is more oxygen in the cell.

The model developed by De Vidts et al. [51] was extended by Wu et al. [53] to include phase reactions in the nickel active material of a Ni–H_2 cell. The phase reactions occurred in two parallel redox paths with different electron transfer numbers: β-$Ni(OH)_2$/β-NiOOH with 1.0 electron transfer and α-Ni(OH)2/γ-NiOOH with 1.67 electron transfer and two connection reactions between them: α-$Ni(OH)_2$/β-$Ni(OH)_2$ and β-NiOOH/γ-NiOOH. Important mechanisms inside a Ni–H_2 cell, such as mass balances of active species, kinetics of electrochemical reactions, and the energy balance of the whole cell, etc. have been considered in the model. The model predictions under different conditions were presented and compared to experimental data. The predicted cell voltage and cell pressure agreed well with the experimental data as shown in Fig. 8. Good agreement between experiment and model was also obtained with the temperature–time curves (not shown here). Based on the simulation results, it was concluded that nickel phase reactions have significant influences on the behavior of a Ni–H_2 cell. Further, some observed phenomena like the capacity variation at different temperatures, KOH concentration change between charge and discharge and cell potential rollover during overcharge were explained with the model.

Wang et al. [54] developed a micro–macroscopic coupled model of electrochemical kinetics and transport phenomena occurring in batteries and fuel cells using the technique of volume averaging. The model accounted for the effects of the micro-scale and interfacial non-equilibrium processes on the macroscopic species and charge transfer. It was shown that solid-state diffusion, ohmic resistance in resistive active materials and electrolytes, and interface passivation can all be incorporated in the present model in a consistent manner. This ultimately allowed for the integration of detailed chemistry and morphology of the electrode/electrolyte interface into a battery model. Gu et al. [55] applied this model to predict discharge and charge behaviors of Ni–Cd and Ni–MH cells. The model predictions were validated against the previous results available in the literature for a Ni–Cd cell and a single MH electrode with good agreement. As compared with the pseudo 2D numerical model, the present model offers a more efficient approach to the modeling of intercalative batteries and can be more easily applied to simulate complex cycles of discharge, rest and recharge as involved in the electric vehicle application. The results of the simulation showed that the Ni–MH cells behave somewhat differently from Ni–Cd cells. In particular, it was observed

that both hydrogen diffusion in MH particles and proton diffusion across the nickel active material can be dominant mechanisms limiting cell performance, depending on the ratio of charge capacities of the two electrodes.

2.4. Modeling of the $Ni(OH)_2$ active material

As the aforementioned examples illustrate, the limitation of previous nickel battery models has been due to the limited understanding of how the nickel hydroxide active material behaves. As improvements have been made in predicting the behavior of the active material, the predictions of the battery models have improved. What follows is a review of models that have been developed to predict various phenomena that occur in the nickel hydroxide active material. This review will include models that describe corrections to the Nernst equation, proton diffusion, and mechanisms of the redox process, including hysteresis. Ultimately, the information that is gained from models of the active material needs to be incorporated into models that couple variations in the microscopic active material with variations in the macroscopic porous electrodes.

2.4.1. Corrections to the Nernst equation

The equilibrium potential of the nickel electrode depends on the state of charge of the electrode as governed by the Nernst equation. However, investigations have shown that for a greater part of the oxidation process the potential is independent of the degree of oxidation [29], a feature that cannot be described by the Nernst equation. In particular, as pointed out by Paxton and Newman [56], two main features define the discharge curves, namely: (i) during most of the discharge, the curve appears Nernstian and (ii) at low states of charge the potential change is steeper than that predicted by Nernstian thermodynamics. This deviation from Nernstian thermodynamics also occurs at high states of charge [57]. Barnard et al. [45] studied the reversible potential of the reaction by re-deriving the Nernst equation using activities in place of concentrations. They studied the effect of the one-parameter Margules and two-parameter Van Laar activity coefficient models on the reversible potential. With these corrections the equilibrium potential takes the form

$$E = E^0 + \frac{RT}{nF}\ln\left(\frac{\theta}{1-\theta}\right) + \frac{RT}{2F}[-2A + 4A(1-\theta) - 2B + 6B(1-\theta) - 3B(1-\theta)^2] \quad (46)$$

with the expression simplifying to the Nernst equation for $A = B = 0$.

The authors demonstrated that changes in the parameters (A and B) can be used to predict the discharge profile of the nickel hydroxide electrode and suggested that the potential of the electrode was held constant by ''pairs of co-existing solid solutions''. Jain et al. [57] recently extended Barnard's model by considering more models for the activity coefficient. They compared their model to experimental data on thin films of nickel hydroxide with 12% cobalt additive and extracted the activity coefficient parameters and the equilibrium potential as a function of temperature. The parameters extracted were for a cathodically deposited film, which has been cycled a few times and would represent the α–γ-phase. Films that have a different structure would require a different set of parameters to represent them. The authors also suggested that the insertion of protons into the lattice occurred in an ordered, non-random fashion.

Fig. 7 shows the equilibrium potential curves obtained by plotting the functionality in Eq. (46). The voltage has been referenced to the voltage of the nickel hydroxide electrode at 50% state of charge. Fig. 7 shows the voltages as described by: (a) the Nernst equation ($A = B = 0$ in Eq. (46)); (b) the one-parameter model ($A = 1.198$, $B = 0$); (c) the two-parameter model ($A = 4.44$, $B = -4.576$), the value backed out by Jain et al. [57] for nickel hydroxide films with 12% cobalt additive, at 27 °C. Increasing the intercalation constant flattens the voltage profile through most of the discharge. In addition, the sharp drop in potential at low and high states of charge is attenuated. Both these features have been seen experimentally in the nickel hydroxide electrode [57]. As expected, the curve follows the Nernst equation through most states of charge.

2.4.2. Proton diffusion

The models that predict the constant current discharge of the cell show that the value used for the diffusion coefficient of protons is critical in predicting the utilization at high discharge rates. Weidner and Timmerman [58] were the first to show the importance of the parameter in terms of its effect on the utilization of the active material. Later, Mao et al. [49] showed that while using a value of 1×10^{-10} cm^2/s ensured complete utilization for a $10C$ discharge, using 1×10^{-12} cm^2/s results in an 80% loss in utilization. Unfortunately, early attempts [44] to evaluate the proton diffusion coefficient resulted in values that varied by three orders of magnitude from 1×10^{-9} to 1×10^{-12} cm^2/s. Therefore, Motupally et al. [59,60] used electrochemical impedance spectroscopy, with the aid of a first-principles model, to measure the diffusion coefficient of protons in a thin film of nickel hydroxide with 12% cobalt additive deposited on a gold substrate. They evaluate the slope of the impedance from their equations and equate it to the experimental data in the transition region (transition from 45° to slope of ∞) to estimate the diffusion coefficient as a function of state of charge. The authors found that the diffusion coefficient data changed as a function of state of charge and followed the trend given by

$$D_{H^+} = D_{NiOOH}\left[\theta + (1-\theta)\left(\frac{D_{Ni(OH)_2}}{D_{NiOOH}}\right)^{1/2}\right]^2 \quad (47)$$

with $D_{Ni(OH)_2} = 6.4 \times 10^{-11}$ cm^2/s and $D_{NiOOH} = 3.4 \times 10^{-8}$ cm^2/s. Eq. (47) is a mixing rule in terms of the root mean square displacement of the diffusing species in a solid

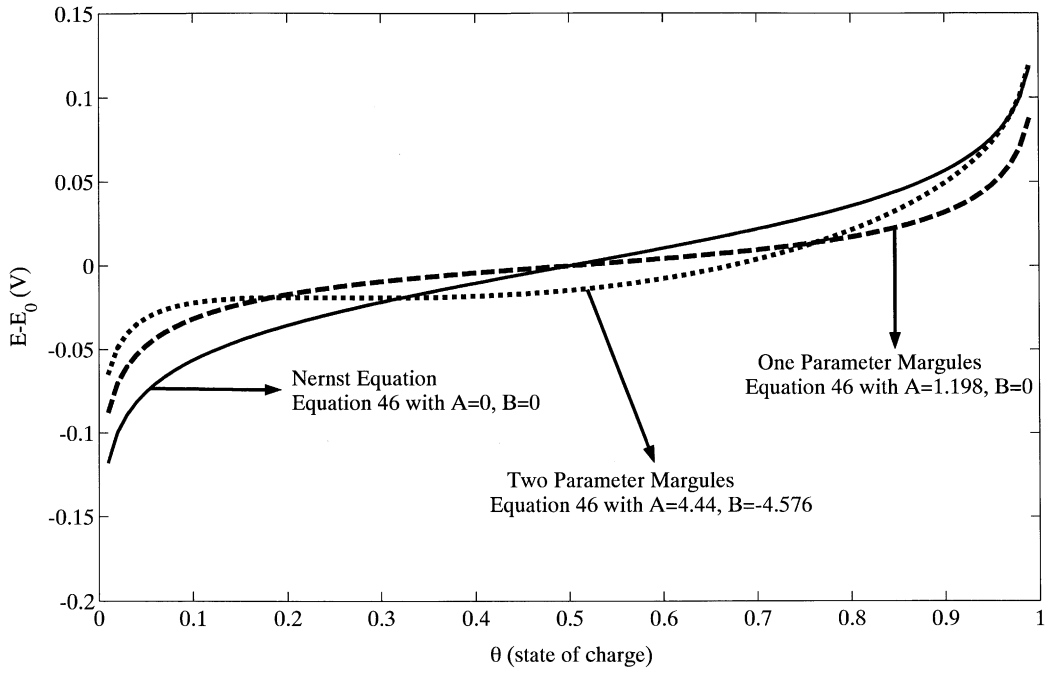

Fig. 7. Equilibrium potential of the nickel hydroxide electrode as a function of state of charge.

solution comprising of a homogeneous mixture of two phases [60].

Motupally et al. [61] also extended the constant-current discharge model by Weidner and Timmerman [58] to include the state of charge dependence of the diffusion coefficient. They compared the two models and found that while on charge, the constant diffusion model compares adequately with the exact solution, there is a significant deviation on discharge. Using the model, the authors predict the utilization of the active material as a function of the charge and discharge currents. They then verify the validity of the proton diffusion functionality with state of charge (Eq. (47)) by conducting experiments on thin films of nickel hydroxide. The utilization of the active material was found to be close to 100% irrespective of the *C*-rate on charge, while there is a significant decrease in utilization on discharge. The excellent agreement between the model and the experiments gives credence to the diffusion coefficients estimated by Motupally et al. [60]. It also validates the assumption that the rate of the nickel hydroxide electrode is governed by transport limitations, as the model by Motupally et al. [61] does not include the kinetics of the nickel reaction. The authors also attempted to estimate a constant diffusion coefficient that would adequately fit the data at all *C*-rates. However, the constant diffusion coefficients used are highly inaccurate in predicting the utilization on discharge and under-predict the utilization on charge.

2.4.3. Reaction mechanism

Loyselle et al. [62] used a point defect approach to describe the active material and proposed that the difference between the two phases was the level of defects. They described the various phases in the active material using the concentration of protons, alkali cations, Ni vacancies, and oxygen present in the lattice, and showed the applicability of the defect model in describing some of the observed phenomenon (e.g. existence of a maximum oxidation state of 3.67). With this information the authors modified the Bode diagram to incorporate these features (for more details on the non-stoichiometric structural model and the modified Bode diagram refer to (44)). Using this modified Bode diagram, Srinivasan et al. [63] developed a procedure that relates the defect parameters to the mass change and capacity. The procedure was used to understand four frequently observed phenomena in the nickel electrode, namely (i) $1.67e^-$ transfer in the first charge while subsequent charges lead to $1e^-$ transfer; (ii) $1e^-$ transfers for the first discharge; (iii) a steady decrease in capacity on both charge and discharge on cycling; (iv) an increase in the total mass of the film on cycling.

Hysteresis is another phenomenon that greatly affects the performance of nickel batteries. The nickel hydroxide electrode is known to exhibit a stable hysteresis loop, with the potential on charge being higher than that on discharge at every state of charge. However, very little beyond this observation has been quantified. Recently, Srinivasan, et al. [64] showed that this hysteresis loop created during a complete charge and discharge (i.e. boundary curves) is not sufficient to define the state of the system. Rather, internal loops within the boundary curves (i.e. scanning curves) can be generated that access potentials between the boundary curves. The potential obtained at any state

of charge, as well as how the material charges and discharges from that point, depends on the cycling history of the material. The implication of this phenomenon is that the potential of nickel-based batteries cannot be used as an indication of the state of charge of the cell. Analysis of the boundary and scanning curves suggest that the electrode consists of a number of individual units or domains, each of which exhibits two or more metastable states. They discussed the cycling behavior of the nickel hydroxide electrode within the context of previously developed theoretical arguments regarding domain theory. Although the specific cause for the metastability in each domain is not understood, considerable insights are provided into the history-dependent behavior of the nickel hydroxide electrode. Finally, they developed an empirical procedure to predict the scanning curves based on the boundary curves.

2.5. Conclusions

A review of the continuum models developed at the University of South Carolina to describe the nickel battery systems was presented. The review also includes models that describe detailed behavior of the nickel hydroxide active material. The methodology used in developing the models, and their relative strengths/weaknesses were discussed. Future improvements to these models will come through a better understanding of how the active material cycles.

Acknowledgements

This work was carried out under a contract with the National Reconnaissance Office for Hybrid Advanced

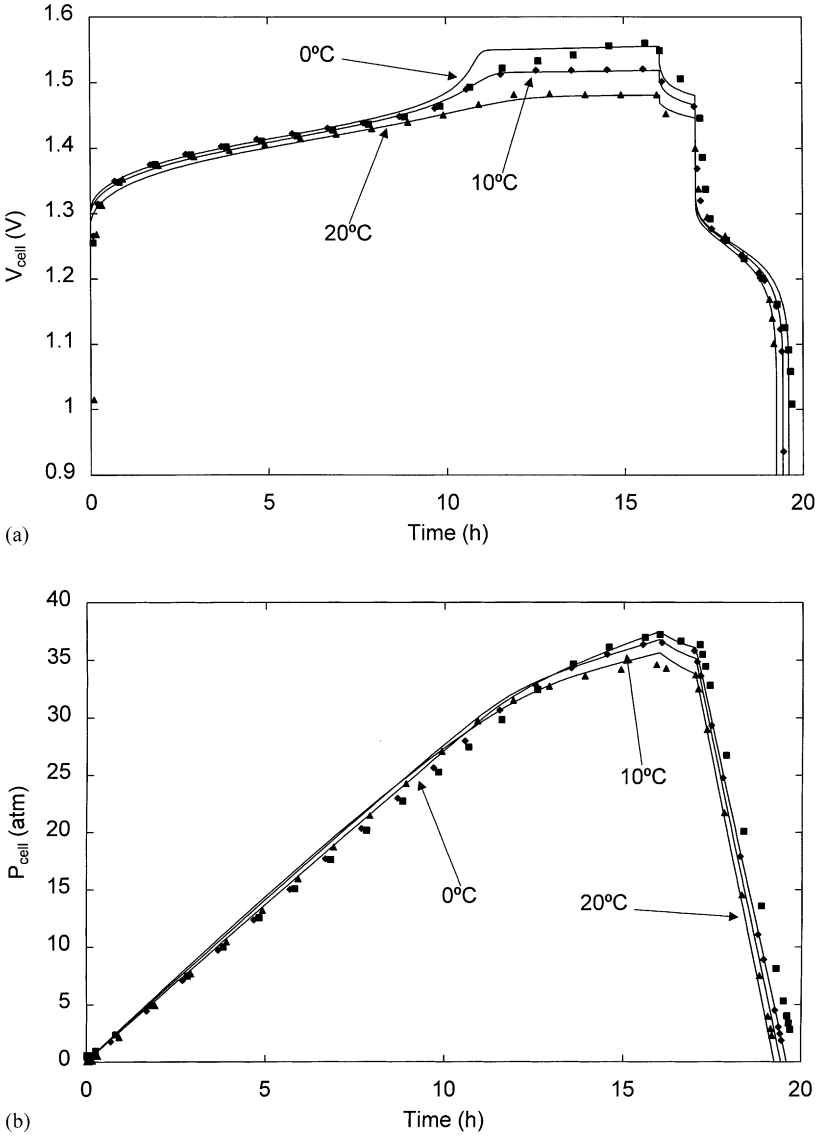

Fig. 8. Comparison of predicted (a) cell potential and (b) cell pressure with experimental data obtained from a 30 Ah cell (reproduced from [53] by permission of The Electrochemical Society).

Power Sources NRO-00-C-1034. The Electrochemical Society is acknowledged for permission to reproduce Figs. 5 and 8.

References

[1] M. Doyle, T.F. Fuller, J. Newman, J. Electrochem. Soc. 140 (1993) 1526.
[2] J.S. Newman, Electrochemical Systems, Prentice Hall, Englewood Cliffs, NJ, 1991.
[3] M. Doyle, J. Newman, A.S. Gozdz, C.N. Schmutz, J.M. Tarascon, J. Electrochem. Soc. 143 (1996) 1890.
[4] C.R. Pals, J. Newman, J. Electrochem. Soc. 142 (1995) 3274.
[5] L. Song, J.W. Evans, J. Electrochem. Soc. 147 (2000) 2086.
[6] Z.H. Wang, W.B. Gu, C.Y. Wang, Extended abstracts, in: Proceedings of the 196th ECS Fall Meeting, Honolulu, Hawaii, 17–22 October 1999, The Electrochemical Society Inc., Pennington, NJ, p. 96.
[7] P.M. Gomadam, J.W. Weidner, R.E. White, J. Electrochem. Soc., Extended Abstracts, in: Proceedings of the 199th ECS Fall Meeting, Washington DC, March 25–30 2001, The Electrochemical Society Inc., Pennington, NJ, #52.
[8] G.G. Botte, B.A. Johnson, R.E. White, J. Electrochem. Soc. 146 (1999) 914.
[9] P. Arora, M. Doyle, A.S. Gozdz, R.E. White, J. Newman, J. Power Sources 88 (2000) 219.
[10] P.M. Gomadam, J.W. Weidner, R.E. White, Extended abstracts, in: Proceedings of the 200th ECS Fall Meeting, San Francisco, CA, 2–7 September 2001, The Electrochemical Society Inc., Pennington, NJ, p. 148.
[11] Q. Guo, V.R. Subramanian, J.W. Weidner, R.E. White, J. Electrochem. Soc. 149 (2002) A307.
[12] M. Doyle, J.P. Meyers, J. Newman, J. Electrochem. Soc. 147 (2000) 99.
[13] P. Arora, M. Doyle, R.E. White, J. Electrochem. Soc. 146 (1999) 3543.
[14] G.S. Nagarajan, J.W. Van Zee, J. Electrochem. Soc. 145 (1998) 771.
[15] A.B. Yu, R.P. Zou, N. Standish, Ind. Eng. Chem. Res. 35 (1996) 3730.
[16] L. Rao, J. Newman, J. Electrochem. Soc. 144 (1997) 2697.
[17] M.W. Verbrugge, B.J. Koch, J. Electrochem. Soc. 143 (1996) 600.
[18] G.G. Botte, R.E. White, J. Electrochem. Soc. 148 (2001) A54.
[19] D. Zhang, B.N. Popov, R.E. White, J. Electrochem. Soc. 147 (2000) 831.
[20] I. Uchida, H. Fujiyoshi, S. Waki, J. Power Sources 68 (1997) 139.
[21] V.R. Subramanian, J.A. Ritter, R.E. White, J. Electrochem. Soc. 148 (2001) E444.
[22] http://nssdc.gsfc.nasa.gov/cgi-bin/database/www-nmc?90-037B.
[23] http://ovonic.com/news/nov13_1997.html.
[24] W. Junger, Patent No. 110,210,113,726,114905 (1899).
[25] A. Salkind, Investigation of the nickel–cadmium cell, Ph.D. Thesis, Polytechnic Institute of Brooklyn, New York, 1958.
[26] http://www.optonline.com/comptons/ceo/00458_A.html.
[27] D. Linden, Handbook of Batteries and Fuel Cells, McGraw-Hill, New York, 1984.
[28] J. McBreen, in: R.E. White, J.O.'M. Bockris, B.E. Conway (Eds.), The Nickel Oxide Electrode, Modern Aspects of Electrochemistry, Plenum Press, New York, 1990.
[29] P.C. Milner, U.B. Thomas, The nickel–cadmium cell, in: C.W. Tobias (Ed.), Advances in Electrochemistry and Electrochemical Engineering, Interscience, New York, 1967.
[30] H. Bode, K. Dehmelt, J. Witte, Electrochim. Acta 11 (1966) 1079.
[31] J. Newman, D. Bennion, C.W. Tobias, Berichte der Bunsengesellschaft fur physikalische Chemie 69 (1965) 608.
[32] J. Newman, D. Bennion, C.W. Tobias, Berichte der Bunsengesellschaft fur physikalische Chemie 70 (1966) 493.
[33] J. Newman, T.W. Chapman, AIChE J. 19 (1973) 343.
[34] A.J. Bard, L.R. Faulkner, Electrochemical Methods Fundamentals and Applications, Wiley, New York, 1980.
[35] D.N. Bennion, Phenomenon at a gas–electrode–electrolyte interface, Ph.D. Thesis, University of California, Berkeley, 1964.
[36] J. Newman, W. Tiedemann, AIChE J. 21 (1975) 25.
[37] F.A. Posey, J. Electrochem. Soc. 111 (1964) 1173.
[38] R. DeLevie, Electrochemical response of rough and porous electrodes, in: C.W. Tobias (Eds.), Advances in Electrochemistry and Electrochemical Engineering, Interscience, New York, 1967.
[39] K. Micka, R. Rousar, Electrochim. Acta 25 (1980) 1085.
[40] K. Micka, R. Rousar, Electrochim. Acta 27 (1982) 765.
[41] K.W. Choi, N.P. Yao, in: S. Gross (Ed.), Proceedings on the Symposium on Battery Design and Optimization, PV 79-1, The Electrochemical Society Proceedings Series, Pennington, NJ, 1979, p. 50.
[42] D. Fan, R.E. White, J. Electrochem. Soc. 138 (1991) 17.
[43] D. Fan, R.E. White, J. Electrochem. Soc. 138 (1991) 2952.
[44] D. Fan, Mathematical modeling of a sealed nickel–cadmium cell, Ph.D. Thesis, Texas A&M University, College Station, 1991.
[45] P. Barnard, C.F. Randell, F.L. Tye, J. Appl. Electrochem. 10 (1980) 127.
[46] P. De Vidts, R.E. White, J. Electrochem. Soc. 142 (1995) 1509.
[47] P. De Vidts, J. Delgado, R.E. White, J. Electrochem. Soc. 142 (1995) 4006.
[48] Z. Mao, R.E. White, J. Electrochem. Soc. 138 (1991) 3354.
[49] Z. Mao, P. De Vidts, R.E. White, J. Newman, J. Electrochem. Soc. 141 (1994) 54.
[50] R. Barnard, G.T. Crickmore, J.A. Lee, F.L. Tye, J. Appl. Electrochem. 10 (1980) 61.
[51] P. De Vidts, J. Delgado, R.E. White, J. Electrochem. Soc. 143 (1996) 3223.
[52] P. De Vidts, R.E. White, J. Electrochem. Soc. 142 (1995) 1509.
[53] B. Wu, R.E. White, J. Electrochem. Soc. 148 (2001) A595.
[54] C.Y. Wang, W.B. Gu, B.Y. Liaw, J. Electrochem. Soc. 145 (1998) 3407.
[55] W.B. Gu, C.Y. Wang, B.Y. Liaw, J. Electrochem. Soc. 145 (1998) 3418.
[56] B. Paxton, J. Newman, J. Electrochem. Soc. 143 (1996) 1287.
[57] M. Jain, A.L. Elmore, M.A. Matthews, J.W. Weidner, Electrochim. Acta 43 (18) (1998) 2649.
[58] J.W. Weidner, P. Timmerman, J. Electrochem. Soc. 141 (1994) 346.
[59] S. Motupally, Measurement of diffusion coefficient of protons in nickel hydroxide films as a function of state of charge, Ph.D. Thesis, University of South Carolina, Columbia, 1994.
[60] S. Motupally, C.C. Streinz, J.W. Weidner, J. Electrochem. Soc. 142 (1995) 1401.
[61] S. Motupally, C.C. Streinz, J.W. Weidner, J. Electrochem. Soc. 145 (1998) 29.
[62] P.L. Loyselle, P.J. Karjala, B.C. Cornilsen, in: R.J. Selman, H.C. Maru (Eds.), Electrochemical and Thermal Modeling of Battery, Fuel Cell and Photoenergy Conversion Systems, PV 86-12, The Electrochemical Society Proceedings Series, Pennington, NJ, 1986, p. 114.
[63] V. Srinivasan, B.C. Cornilsen, J.W. Weidner, in: G. Halpert, M.L. Gopikanth, K.M. Abraham, W.R. Cieslak, W.A. Adams (Eds.), Selected Battery Topics, PV 98-15, The Electrochemical Society Proceedings Series, Pennington, NJ, 1999, p. 31.
[64] V. Srinivasan, J.W. Weidner, J. Newman, J. Electrochem. Soc. 148 (2001) A969.